actuators

Article

Combined Passive/Active Flow Control of Drag and Lift Forces on a Cylinder in Crossflow Using a Synthetic Jet Actuator and Porous Coatings

Gearóid Farrell , Michael Gibbons and Tim Persoons *

Department of Mechanical, Manufacturing & Biomedical Engineering, Trinity College Dublin, The University of Dublin, D02 PN40 Dublin, Ireland; farrelg4@tcd.ie (G.F.); michael.gibbons@tcd.ie (M.G.)
* Correspondence: tim.persoons@tcd.ie; Tel.: +353-1-896-1936

Abstract: This paper combines a synthetic jet actuator (SJA) and a leeward porous coating to alter the aerodynamic forces on a cylinder in crossflow at $Re = 4.2 \times 10^4$. While SJAs and porous coatings are known to be effective flow control methods in isolation, their combined effect has not been studied. A 2D numerical model was created of a cylinder with a SJA at 90° and 100° leeward porous coating. The model was validated using accompanying water tunnel tests. The combined model was tested for dimensionless frequencies $0.15 < f^+ < 4$ and compared to reference models. For $f^+ < 1$, using only the SJA increases the cylinder drag coefficient (C_d). Combining a porous coating with the SJA in that regime lowers the C_d values by 15–21%, and causes an overall reduction in C_d compared to the smooth cylinder baseline case. However, using only the porous coating causes a superior 35% reduction in C_d. For $f^+ > 1$, the combined SJA and porous coating configuration did not differ from the SJA only configuration, achieving the largest drag reduction of 45% at $f^+ = 4$. The flow control mechanisms of the SJA and porous coating do not combine constructively in this current setup. However, the porous coating is beneficial for $f^+ < 1$, causing an overall drag reduction even when the active SJA tends to increase drag.

Keywords: drag reduction; oscillating lift; porous media flow; vortex shedding; synthetic jet; experimental fluid dynamics; water tunnel; computational fluid dynamics; URANS; k-ω SST

check for updates

Citation: Farrell, G.; Gibbons, M.; Persoons, T. Combined Passive/Active Flow Control of Drag and Lift Forces on a Cylinder in Crossflow Using a Synthetic Jet Actuator and Porous Coatings. *Actuators* **2022**, *11*, 201. https://doi.org/10.3390/act11070201

Academic Editor: Luigi de Luca

Received: 14 June 2022
Accepted: 17 July 2022
Published: 19 July 2022

Publisher's Note: MDPI stays neutral with regard to jurisdictional claims in published maps and institutional affiliations.

Copyright: © 2022 by the authors. Licensee MDPI, Basel, Switzerland. This article is an open access article distributed under the terms and conditions of the Creative Commons Attribution (CC BY) license (https://creativecommons.org/licenses/by/4.0/).

1. Introduction

There are many examples of engineering designs incorporating cylindrical components, from aircraft landing gears to train pantographs. These bluff bodies produce unwanted fluctuating aerodynamic forces and wakes [1]. This can lead to acoustic noise or structural challenges. The inevitable drag force requires energy to overcome. The field of flow control aims to combat these issues by manipulating the flow field around the components [2]. A flow control method can be classified as either active or passive, where the former adds energy to the system while the latter does not [3]. This paper focuses on the combined performance of an active flow control method (synthetic jet actuator, SJA) and a passive method (porous surface coating). Each has been studied previously in isolation, with numerous studies demonstrating drag reduction using SJAs [4–7] and porous coatings [8–10] when applied to cylinders in crossflow. Porous coatings around cylinders have also been shown to largely suppress oscillating lift forces [11] and reduce noise [12]. Therefore this current study focuses on altering the drag coefficient (C_d) and the root-mean-square (RMS) lift coefficient ($C_{l(rms)}$) of a cylinder using these technologies.

1.1. Synthetic Jet Actuators

SJAs impart momentum to a flow through a train of vortices generated by cyclically ingesting and ejecting surrounding fluid through an orifice [13]. By 'synthesising' this jet from the surrounding fluid, they operate without net mass input, avoiding the need for an auxiliary fluid supply. SJAs can make large-scale alterations to the flow field relative to its characteristic length scale [13]. The layout of a SJA consists of an orifice with width d, a cavity, and an actuator to drive the fluid motion, which can be piezoelectric, electromagnetic, acoustic, or a mechanical device [14]. The layout of the SJA used in this current study is shown in Figure 1a for reference. The vortex train is generated through successive expulsion phases, in which the actuator drives fluid out of the cavity through the orifice, rolling up to form vortex rings [15]. The vortex ring moves away from the orifice provided its position and momentum is such that it will not be re-ingested during the following ingestion phase [13]. During the expulsion phase, the addition of momentum can re-energise a low-energy boundary layer region while, during the ingestion phase, low-momentum fluid is removed from the boundary layer. Therefore, both phases may help delay separation of the boundary layer. This increases the pressure on the lee of the cylinder and reduces the pressure drag [16].

This study uses the following parameters to describe the synthetic jet and crossflow: (i) stroke length L_0 and (ii) jet Reynolds number Re_j [13,17], as well as (iii) the dimensionless frequency f^+ and (iv) the momentum coefficient C_μ [4,6]. The stroke length, L_0 (or its dimensionless equivalent $\bar{L}_0 = L_0/d$) represents the length of the fluid slug ejected by the SJA. L_0 is defined as the integral of $u_m(t)$, the spatially-averaged orifice fluid velocity over the ejection phase. Re_j is defined as $Re_j = U_0 d/\nu$, where U_0 is the average ejection velocity over a full jet cycle, and ν represents the fluid kinematic viscosity. These parameters are related as shown by Equation (1), where f is the SJA actuation frequency [17].

$$U_0 = fL_0 = f\int_0^{\frac{1}{2f}} u_m(t)\,dt \tag{1}$$

$\bar{U}$ is the average ejection velocity, $\bar{U}_0 = 2U_0$. An alternate version of the jet Reynolds number is given by $\bar{R}e_j = \bar{U}_0 d/\nu$. Holman et al. [17] created a criterion for SJ formation in quiescent or still flow given by $1/Sr_j = \bar{R}e_j/S_j^2 < K$, where the jet Stokes number S_j and Strouhal number Sr_j are given by $S_j = \sqrt{2\pi\, fd^2/\nu}$ and $Sr_j = fd/U_\infty$, respectively. Here, the jet formation constant is taken as $K = 1$ for a two-dimensional SJA. The dimensionless frequency f^+, is given by $f^+ = f/f_s$ [6], the ratio of the SJA frequency f to the cylinder vortex-shedding frequency f_s. The momentum coefficient is given by $C_\mu = 2dU_0^2/DU_\infty^2$, where D is the cylinder diameter [6]. C_μ is a measure of the relative strength of U_0 to the free-stream velocity U_∞, and is closely related to the velocity ratio VR given by $VR = U_0/U_\infty$. This quantity characterises the trajectory of the synthetic jet (SJ) in the boundary layer [18]. The SJA angle, θ, is the angle between the front stagnation point of the cylinder and the SJA orifice, as shown in the test sample in Figure 1a.

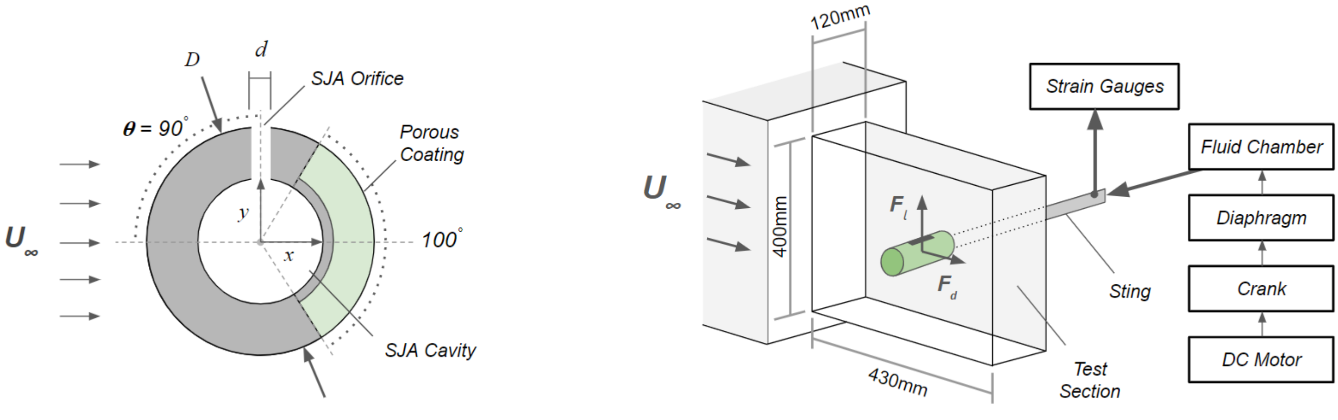

(**a**) (**b**)

Figure 1. Experimental apparatus used in current study (**a**) Combined SJA and porous coating test sample (**b**) Water tunnel test section and SJA setup (full details in Section 2.1).

The flow structures of SJAs embedded in finite wings have been studied [19] and they have been shown to be capable of reducing the severity of boundary layer separation on finite wings with deflected control surfaces [20]. SJAs have also been studied for controlling the behaviour of water sprays [21]. However, the current study focuses on SJAs embedded in cylinders in crossflow. Amitay et al. [4] used a 2D smoke tunnel to study the flow field effects of embedding two neighbouring SJAs in a cylinder in crossflow (Re = 4 × 10^3 and Re = 7.5 × 10^4) for a range of SJA angles (0–180°). At the higher Reynolds number, f^+ was varied between 11.5 and 20. The SJAs were found to create a closed re-circulation flow near the surface of the cylinder, acting as a 'virtual' surface and displacing streamlines outside of the boundary layer. The pressure distribution around the cylinder saw an increase in pressure at the lee for angles between 0° and the separation point. The maximum drag reduction was 30% for a SJA position of $\theta = 100°$ and C_μ = 6 × 10^{-4}. There was no effect of f^+ on the pressure distribution in this range. The observed virtual surface was also reported by Feng et al. [22] for an SJA at $\theta = 0°$, altering the apparent aerodynamic shape of the body.

Catalano et al. [6] used DNS and LES to optimise SJAs embedded in a cylinder in crossflow for drag reduction. At $Re = 500$, a drag reduction of 6% was found using f^+ = 5 and $\theta = 93.9°$. At $Re = 3900$, a drag reduction of 13% was found for f^+ = 9.2 and $\theta = 85.12°$. This agrees with Amitay et al. [4], who observed maximum drag reduction when the SJA is placed close to the separation point.

The above studies focused on SJA frequencies larger than the natural vortex shedding frequency ($f^+ > 1$). By contrast, Tensi et al. [23] studied experimentally the effect of SJAs at lower frequencies (f^+ = 0.33, 0.5, 1) at $\theta = -60°$, $-112.5°$ and 180°. They showed that the SJA can significantly modify the flow even for a small value of C_μ = 6.48 × 10^{-3}; much lower than would be needed for an equivalent continuous jet with C_μ = $O(1)$. For a SJA angle of $\theta = -112.5°$ (i.e., near the separation point), Tensi et al. [23] showed delayed separation and a reduced re-circulation zone when $f^+ \approx 1$. They also found an increased drag coefficient C_d for the range of f^+ and C_μ tested. This highlights the influence of f^+ on the drag reduction effect of SJAs.

The work of Fuijsawa and Takeda [5] helps to bridge the findings of Tensi et al. [23] and other studies focusing on dimensionless frequencies above unity [4,6,16,22]. They studied the effect of SJAs for $Re = 9 \times 10^3$ for moderate-to-high frequencies, f^+ = 1–5. For θ close to 90°, there was a significant increase in C_d and $C_{l(rms)}$ for $f^+ = 1, 2$. This agrees with the findings of Tensi et al. [23], who found an increase in C_d for $f^+ \leq 1$ for a similar SJA position. For values of $f^+ > 3$, Fuijsawa and Takeda [5] found a reduction in C_d up to 30% for $\theta = 90°$, C_μ = 3.6 × 10^{-3} and f^+ = 4. They attributed this to the SJA exciting the frequency of shear layer instabilities, as did Hsaio and Shyu [24]. This was further supported by Glezer et al. [25], who studied the effect of an SJA at 60° for 1.14 < f^+ < 4 and 12 < f^+ < 24. In the lower range of f^+, a maximum drag reduction of 17% was achieved for f^+ = 4. Across all frequencies tested, there was also an increase in lift coefficient.

Feng et al. [16] showed experimentally that a SJA placed at $\theta = 180°$ can reduce C_d by 29% for $Re = 950$. This is confirmed by Greco et al. [7] who showed a drag reduction of 35% for $\theta = 180°$ with $f^+ = 0.98$ and $C_\mu = 0.0108$. Across a range of f^+ or C_μ values (f^+ = 0.49, 0.98, 1.96 and C_μ = 5 × 10^{-3}, 10.8 × 10^{-3}, 21.6 × 10^{-3}), they found consistent drag reduction and also showed that an increase in f^+ or C_μ reduced the extent of the wake region.

1.2. Porous Coatings

Porous coatings have been studied for various applications beyond cylinders in cross-flow. Bruneau et al. [26] demonstrated that partial porous coatings can reduce drag on Ahmed bodies by up to 45%. Teruna et al. [27] showed that a porous trailing edge on a NACA0018 aerofoil can reduce aerodynamic noise by up to 7 dB. Porous coatings have also been studied for reducing noise produced by vortex shedding for bluff bodies such as cylinders, as well as reducing their drag coefficients in certain cases.

Bhattacharyya and Singh [28] numerically studied the effect on cylinder drag of full porous coatings in laminar flow as a function of thickness and permeability. By correcting for the diameter increase from the coating, they found drag coefficient reductions of up to 32.34%. Bruneau and Mortazavi [11] used a full porous coating for $2400 < Re < 3000$ to regularise vortex shedding and reduce flow-induced vibrations, resulting in a 72% reduction in $C_{l(rms)}$ at $Re = 1.5 \times 10^5$. This agrees with Sueki et al. [29], who showed experimentally that a full porous coating for $4.6 \times 10^4 < Re < 8.3 \times 10^4$ reduces aerodynamic noise and increases the size of the zero velocity region in the cylinder wake, attributing this to the porous coating reducing fluid momentum in the wake and subduing vortex shedding. Bathla and Kennedy [12] showed experimentally that high porosity coatings significantly reduced turbulence in the wake, with a 95% porosity coating offering a 70% reduction in turbulence compared to a smooth cylinder. Hu et al. [30] found numerically that *partial* porous coatings around the separation point can reduce drag by 30% .

Naito et al. [31] found differing results in their numerical simulations of porous coated cylinders: for a wide range of Reynolds number (100–10^5), the coating increased C_d. However, at $Re = 10^5$, $C_{l(rms)}$ tended to zero. The fluid dissipates a large amount of energy in the porous layer and, as it emerges from the coating, generates a stable low-velocity and low-pressure region on the leeward side of the cylinder. This stabilises the detached shear layer and reduces aerodynamic force fluctuations.

Zhang et al. [8] found numerically a drag reduction of up to 26% using a full uniform porous coating of 95% porosity, as well as reduced lift fluctuations at $Re = 4.7 \times 10^4$, contrary to the findings of Naito et al. [31] at this flow regime. They also achieved a 20% drag reduction using a lower porosity non-uniform coating by adding a higher porosity region near the separation point. Lower-momentum flow emerging from the coating was seen to increase the pressure in the lee.

Klausmann and Ruck [10] performed a comprehensive experimental study into the drag reduction effect of partial porous coatings in the lee of a cylinder. Wind tunnel tests at $3 \times 10^4 < Re < 1.4 \times 10^5$ were conducted with varying porosity (10 Pores Per Inch (PPI), 20 PPI and 30 PPI), coating thickness (3 mm, 5 mm and 10 mm), and coating angle (40°, 70°, 100° and 160°). Across all tests, a drag reduction of 7.7–13.2% was observed. In the wake, the porous coating reduced the mean velocity components, normal stresses, turbulent kinetic energy, and velocity fluctuations. The coating delayed vortex shedding, which caused a pressure increase in the lee as shown by others [28,29]. They attributed this to the 'base bleed' effect of the porous coating, in which fluid emerges from the coating into the wake. Base bleed has been shown to delay vortex shedding and reduce pressure drag in other bluff body studies [32–34]. The optimum coating angle was found to be 100°, with a drag reduction of 13.2%. Guinness and Persoons [9] characterised the porous coating used by Klausmann and Ruck [10] and numerically studied the same conditions in ANSYS Fluent. The 2D RANS model produced similar results yet suggested a maximum drag reduction at a porous coating angle of 70° as opposed to 100° found by Klausmann and Ruck [10].

1.3. Summary

The conditions of the aforementioned studies most relevant to this current study are summarised in Tables 1 and 2 and Figure 2 schematically shows the corresponding ranges of f^+ and SJA angle θ. The plot shows the approximate regions where either drag reduction or drag increase dominated within the parameters studied. Both SJAs and porous coatings offer advantages in terms of flow control. SJAs can effectively reduce cylinder drag when positioned near the separation point and $f^+ > 1$ [4–6,25]. Cylinders do not require full porous coatings for effective flow control; a partial coating on the lee is sufficient to significantly reduce drag [9,10]. To the best of the authors' knowledge, this study is the first to combine a SJA and porous coating for flow control around a cylinder in crossflow using experimental and numerical techniques. Based on the optimal SJA settings found by Fuijsawa and Takeda [5] and Glezer et al. [25], and the optimal porous coating parameters by Klausmann and Ruck [10], this paper studies a cylinder in crossflow at $Re = 4.2 \times 10^4$ with an embedded SJA for a range of frequencies $0.15 \leq f^+ \leq 4$ and a constant $C_\mu = 3.6 \times 10^{-3}$ at an angle of 90° in combination with a leeward porous coating of 100° using experimental and numerical techniques.

Table 1. Summary of most relevant literature of SJAs on cylinders in crossflow.

Author	Study	θ (°)	C_μ ($\times 10^{-3}$)	f^+	Re	$\Delta\, C_d$
Amitay et al. [4]	Exp.	0–180	0.03–0.6	11.5–20	4000, 7.5×10^4	−30%
Catalano et al. [6]	Num.	60–120	6.5	2–14	500, 3900	−13%
Tensi et al. [23]	Exp.	(−)60–180	0.81–6.48	0.33–1	1.0×10^5	+36%
Fujisawa & Takeda [5]	Exp.	60–120	0.41–6.5	1–5	9.0×10^3	−30%
Glezer et al. [25]	Exp.	60	0.6	1.15–23	7.6×10^4	−17%
Current study	Num.	90	3.6	0.15–4	4.2×10^4	−46%

Table 2. Summary of most relevant literature of porous coatings around cylinders in crossflow.

Author	Study	Coating	Turb. Model	Re	$\Delta\, C_d$	$\Delta\, C_{l(rms)}$
Bruneau et al. [11]	Num.	Full	DNS	2400–3×10^4	-	−75%
Naito et al. [31]	Num.	Full	DNS/LES	100–1×10^5	+70%	−73%
Zhang et al. [8]	Num.	Full	k-ω/LES	4.7×10^4	−30%	-
Klausmann & Ruck [10]	Exp.	Partial	-	3×10^4–1.4×10^5	−13%	-
Guinness & Persoons [9]	Num.	Partial	k-ω	4.2×10^4	−15%	−54%

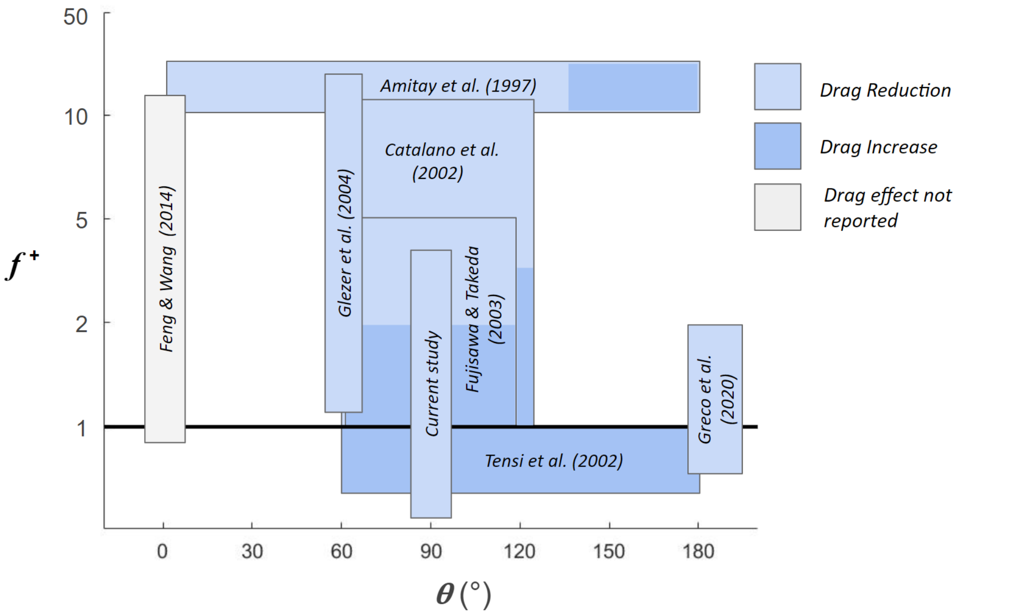

Figure 2. Summary of literature on drag reduction of cylinders in crossflow using SJAs [4–7,22,23,25]. Each box in the f^+, θ space represents the limits of these variables investigated.

2. Materials and Methods

2.1. Experimental Setup

The experiments are conducted in a closed-loop water tunnel which also comprises a modular synthetic jet actuator (SJA) [35]. Figure 1b shows a simplified layout of this setup. A test section measuring 400 × 430 × 120 mm^3 can achieve freestream velocities up to 3 m/s at turbulence intensities < 1%. Test samples are mounted to a hollow sting, clamped at the other end with 4 strain gauges at its base for measuring drag and lift forces. The SJA consists of a small fluid chamber connected the water tunnel via the hollow sting, which produces a jet from an orifice embedded in the mounted test sample. A diaphragm in the fluid chamber is driven by an eccentric crank and DC motor. Since the crank connecting rod is much longer than the eccentricity e, the diaphragm motion is quasi sinusoidal. The actuation frequency, f, is controlled with the DC motor speed with values between 4–25 Hz. The SJ stroke length, L_0, is a function of the swept distance of the diaphragm during the expulsion phase, L_d. L_d is related to the eccentricity of the crank, e by $L_d = 2e$. Using continuity, L_0 and L_d can be related using $L_0 = L_d A_d k_d / A_o$, where A_d is the diaphragm area, A_o is the orifice area and $k_d = 0.55$ is the usable fraction of the diaphragm. This value of k_d is based on previous PIV work on SJAs in the current experimental setup and allows the analytical orifice velocity to match the experimentally found values [35].

The strain gauges are arranged in a half bridge II configuration, with gauges placed at 90° increments around the sting. The vertically aligned gauges measure the lift force, F_l, while the horizontally aligned gauges measure the drag force, F_d. The strain gauge outputs are read with a National Instruments NI-9237 data acquisition module and cDAQ-9178 chassis, and converted to force values in LabVIEW. This conversion is done using a calibration curve produced by hanging a series of known weights from the test sample centroid and recording the outputs of the strain gauges. This process is done for the positive and negative drag and lift forces by rotating the sting in 90° increments.

The free-stream velocity, U_∞, in the test section is found using an ultrasonic volumetric flow meter mounted downstream of the propeller and a Pitot tube placed in the test section outside of the cylinder wake. The readings from both sensors were compared to ensure a correct measurement of the instantaneous $U_\infty(t)$.

2.2. Test Samples

The test samples contain a SJ orifice and an embedded porous coating on its lee. The cylinders are 20 mm in outer diameter and 119 mm long to allow clearance with the test section walls. The SJ orifice is rectangular, measuring 1×40 mm^2 in cross-section, and an inner cavity of 11.5 mm diameter. The embedded porous coating covers 100° of the cylinder lee and has thickness of 15% the cylinder diameter.

Two test samples are made, shown in Figure 3a: (i) one containing only a SJ orifice (top) and (ii) another containing a SJ orifice and porous coating (bottom). By deactivating the SJA rig during testing these samples can be used as a 'smooth baseline' case and 'porous coating only' case, respectively. The test samples are manufactured as two primary parts—the main body and the porous coating—and then assembled. The main body is printed in PLA using a Ultimaker 2+ FDM printer, while the porous coating is manufactured using an Anycubic PHOTON SLA printer, in line with the work of Bathla and Kennedy [12]. As shown in Figure 3b, the main body is printed in two parts and assembled inside the test section to allow sample mounting through a small window on top of the rig. Samples requiring a coating include a 3 mm recess in their leeward sides to receive a porous coating.

The porous coatings used in this current study are based on a regular lattice of a unit cell. Bathla and Kennedy [12] found that the self-supporting Kelvin cell was superior in terms of lattice manufacturing to the cubic cell. However, this current study uses a cubic unit cell as it produces coatings with a higher porosity that are easier to clean prior to curing and are therefore less prone to resin blockages. The lattice modelling package nTopology is used to produce meshes of these lattice structures which are then sliced and 3D printed. The nTopology package allows for a given CAD body to be filled with a thickened lattice built from a specified unit cell. A porous coating was manufactured with 1 mm cells and 0.3 mm trusses. The structure has a porosity of about 80%, similar to the value used by Guinness and Persoons [9] and a PPI value of 25.4, which is in the range of values tested by Klausmann and Ruck [10]. The coating has a 0.3 mm wall along its back and sides to allow it to be glued into the main body of the test sample without glue permeating into the structure.

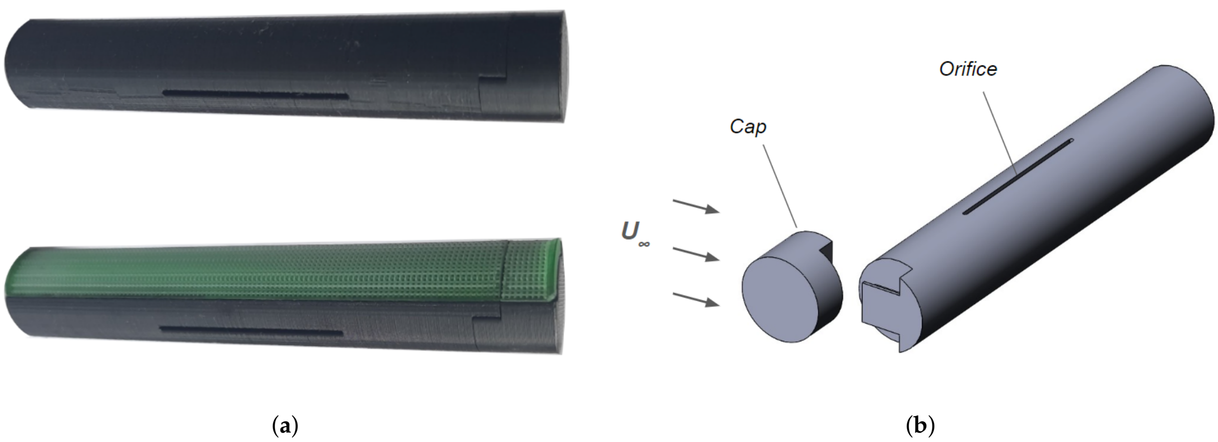

Figure 3. Test samples used in experimental phase of current study (**a**) Smooth baseline and SJO configuration (top), SJPC and PCO configuration (bottom), (**b**) schematic showing assembly of cap and main body.

2.3. Numerical Setup

All simulations are carried out using a pressure-based solver in ANSYS Fluent 2021 R2. A crossflow of incompressible fluid with a Reynolds number of 4.2×10^4 is used for comparison with Klausmann and Ruck [10] and Guinness and Persoons [9]. The domain is representative of the water tunnel test section. A 2D unsteady Reynolds-averaged Navier-Stokes (URANS) model is used [9]. The SST k-ω turbulence model is used as it combines the advantages of the k-ω and the k-ϵ models, as well as being suited to modelling adverse pressure gradients and boundary separation [36,37]. The 'Porous Media' model in Fluent is used to model the leeward porous coating. The SJA is modelled using a time-varying velocity-inlet boundary condition at the actuator surface. Guinness and Persoons [9] implemented a pressure-velocity coupled solver. However, this current study involves a SJA and therefore uses the SIMPLE solver to accommodate mass-flux across the actuator surface [38].

2.4. Porous Medium Model

The porous media model in Fluent does not represent the structure of the porous medium. Instead, it models the pressure drop of fluid in this region as a continuum by adding a momentum source term, which is shown in its most general form in Equation (2). Here, S_i is the source term for the ith momentum equation in the x, y, z directions, $|v|$ is the velocity magnitude and D and C are prescribed matrices [38].

$$S_i = -(\Sigma_{j=1}^{3} D_{ij}\mu\, v_j + \Sigma_{j=1}^{3} C_{ij}\frac{1}{2}\rho\, |v|v_j) \tag{2}$$

This equation can be simplified for a homogeneous porous medium, given by Equation (3). C and D now become diagonal matrices containing $1/K$, the viscous resistance factor and C_2, the inertial resistance factor, respectively. The first term on the right hand side represents viscous losses while the second represents inertial losses.

$$S_i = -(\frac{\mu}{K}v_i + C_2\frac{1}{2}\rho\, |v|v_i) \tag{3}$$

Values of $1/K$ and C_2 representative of the porous medium in the test samples were found using the procedure detailed in the Fluent porous media model manual [38]. A 3D numerical model was created to simulate flow through a single row of cells representative of the test sample porous coating. A range of velocities ($O(0.1-1)$ m/s) was applied and the subsequent pressure drop across the row of cells was measured. A second order fit was applied to the pressure drop and velocity data. By comparing the first and second order coefficients in the fitted equation and a one dimensional version of Equation (3), values of $1/K = 8 \times 10^7$ m^{-2} and $C_2 = 1000$ m^{-1} were derived.

2.5. SJA Model

The actuation of SJAs has been modelled in various ways. Catalano et al. [6] modelled the actuator as a time-varying velocity inlet while other studies have modelled it as a dynamic surface [39,40]. A time-varying velocity inlet approach is used in this study on a source area within the inner cavity of the cylinder (surface [D] in Figure 4b), as it has been shown by Jain et al. [40] to achieve a very similar velocity profile at the orifice outlet to dynamic actuator models, while requiring only around half the simulation time [40].

Equation (4) is coded as a user-defined function, UDF, in C to apply a sinusoidal velocity, U_d, to the actuator surface. A sample of the UDF code used in this study is provided in Appendix A. This profile approximates the movement of the experimental SJA. Equation (4) produces a peak orifice velocity, $U_{p(o)}$, which can be related to U_0 by $U_{p(o)} = U_0\pi$. The peak actuator velocity, $U_{p(d)}$, is related to $U_{p(o)}$ as $U_{p(d)} = U_{p(o)}(A_0/A_d)$, where A_o and A_d are the orifice and actuator widths respectively. This expresses U_d in terms of the desired values of L_0 and f for the SJA.

$$U_d = L_0 f \pi \frac{A_o}{A_d} sin(2\pi f t) \quad (4)$$

2.6. Domain and Boundary Conditions

The computational domain is shown in Figure 4a with all salient dimensions normalised by $D = 20$ mm, the cylinder diameter. The fluid domain is 21.5D in width and 20D in height. The cylinder is positioned 4.8D from the left edge of the domain at the vertical midpoint. The orifice width d is 1 mm, with the cavity diameter equal to 11.5 mm, identical to the experimental test cases. While the actuator surface shown is not a real surface in the test samples, it was added to model the behaviour of the SJA. The boundary conditions and mesh of the outer domain and cylinder are shown in Figure 4.

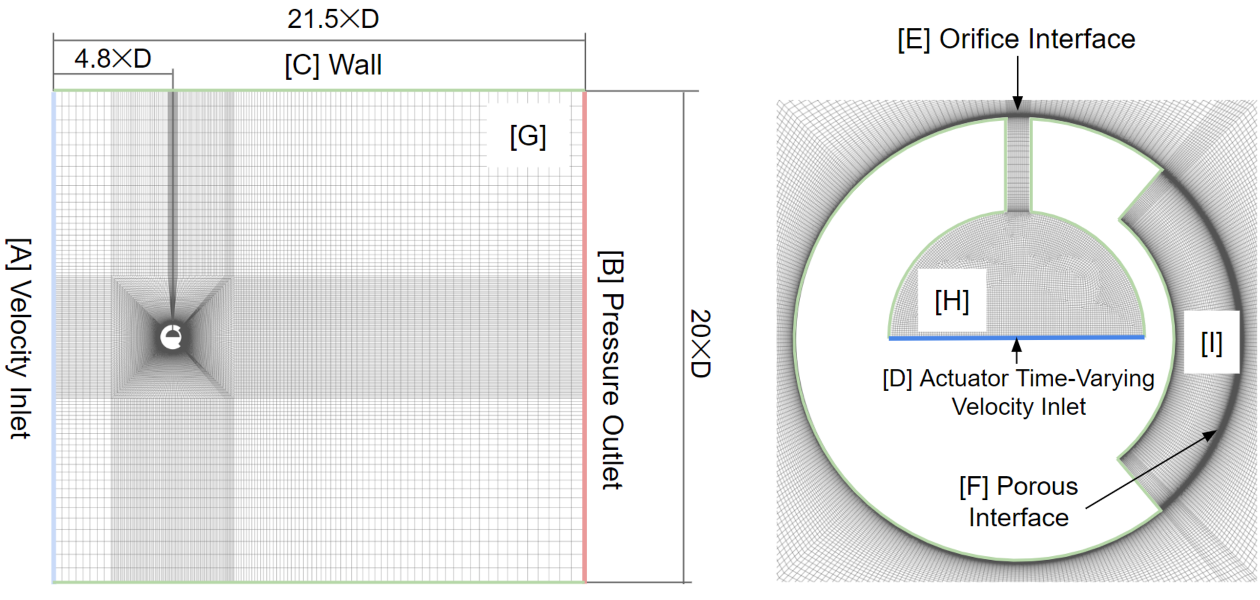

(**a**) (**b**)

Figure 4. Mesh and boundary conditions for the CFD model of the cylinder in cross-flow with combined SJA and porous coating. (**a**) Outer domain and (**b**) detailed view of the cylinder.

For all simulations an inlet velocity of $U_\infty = 2.11$ m/s is set at inlet [A] to produce $Re = 4.2 \times 10^4$ based on the cylinder diameter, with [B] set as a zero pressure outlet. The aforementioned UDF is applied to the actuator surface [D] as a velocity-inlet. The porous media model is applied to the porous coating, marked as [I]. [E] and [F] represent the orifice exit boundary and the fluid-porous boundary respectively. Each of the boundaries [E] and [F] can be set to either a solid wall or internal boundary which allows for fluid to flow across it. The three primary models used in this current study can be obtained by varying these interfaces:

- 'Combined SJA and Porous Coating' (SJPC) model by making both [E] and [F] internal boundaries.
- 'Porous Coating Only' (PCO) model by making [E] a wall and [F] an internal boundary.
- 'SJA Only' (SJO) model by making [F] a wall and [E] an internal boundary.

The PCO and SJO models are created to model the flow control effect of the SJA and the porous coating individually for a given set of parameters. This helps to understand the results of the combined SJPC model. The acronyms established here will be used for the remainder of this study to refer to these setups.

2.7. Mesh Development

Similar to Guinness and Persoons [9], the square region around the cylinder is modelled as a structured quadrilateral mesh. A bias was applied to these radial lines towards the cylinder such that a first cell height of 9×10^{-6} m was obtained at the cylinder surface. This ensured a value of $y^{+} < 1$ at the cylinder wall [36]. The orifice and porous coatings also contain structured quadrilateral meshes that are biased toward their interfaces with the outer fluid domain. Within the semicircular cavity, an unstructured mesh of mixed elements was used to avoid highly skewed elements near the orifice.

ANSYS Fluent uses an implicit formulation for solving transient simulations, allowing Courant numbers between 20–40 for accurately simulating transient flow behaviour [38]. Initial simulations showed a near-wall cell size of 9×10^{-6} m and a time-step of 1×10^{-4} s was suitable to maintain the largest Courant numbers in the domain within this range. A time-step was deemed to have converged when the continuity residual reached 2×10^{-4} and the remaining residuals reached 1×10^{-4}.

2.8. Verification and Validation

A mesh refinement study was performed using a smooth cylinder variation of the above mesh ([E] and [F] set as wall boundaries) following the Richardson extrapolation (RE) method [41]. Three successively finer meshes were made, termed 'Coarse', 'Medium', and 'Fine' which contained 51,200 (N_3), 71,600 (N_2), and 100,600 (N_1) elements, respectively. For each mesh the time-averaged C_d was measured for a crossflow of $Re = 4.2 \times 10^4$. The pressure coefficient, C_p is defined as $C_p = 2(p_s - p_0)/\rho\, U_\infty^2$, where p_s is the local static pressure and p_0 is the reference atmospheric pressure [1]. Ignoring the contribution of skin friction, as is reasonable at this high Reynolds number, a value of the pressure drag coefficient C_d can be calculated as $C_d = 1/2 \int_0^{2\pi} C_p\, cos(\theta)\, d\theta$ [1]. The grid convergence ratio, r_g, was found to be 0.685, meaning that the solution is converges monotonically across the meshes. The grid convergence index GCI_{fine} found is 1.41%, which can be used as a minimum estimate of error for any subsequent numerical results.

The fine mesh produces a C_d of 1.194, for a 12 h simulation time, while the coarse mesh produced a C_d of 1.18, for a 6 h simulation time. The coarse mesh is therefore used for the remaining simulations, as it requires half the simulation time of the fine mesh and differs in C_d values by only 1.18%.

Values of C_d, $C_{l(rms)}$ and Sr found for the coarse mesh are compared to experimental and numerical values from the literature in Table 3. The value of C_d agrees well. However, it tends to underestimate the drag coefficient. The value of $C_l(rms)$ agrees well with that found numerically by Liu et al. [42]. However, the vortex shedding Strouhal number Sr is significantly different. This may be due to the much larger Reynolds number used in that study.

Table 3. Comparison of key flow characteristics for smooth cylinder at $Re = 4.2 \times 10^4$ in the current study and the literature.

Author	Re	C_d	$C_{l(rms)}$	Sr
Current	4.2×10^4	1.18	0.969	0.255
Klausmann & Ruck [10]	4.2×10^4	1.24	-	-
Roshko [43]	4.2×10^4	1.2	-	-
Liu et al. [42]	9.3×10^4	1.31	0.88	0.196

3. Results

3.1. Experimental Results

This section describes the tests carried out to validate the numerical model developed in this current study. Due to limitations of the experimental setup, a lower Reynolds number in the sub-critical flow regime of $Re = 3.0 \times 10^4$ was used in all tests. For all tests, 30 s measurements with a sampling rate of 100 Hz were taken of the outputs of the strain gauges, flow meters, and IR frequency sensor. In cases involving the SJA, the desired frequency of the SJA was achieved by setting the voltage and current applied to the DC motor.

3.1.1. Uncertainty and Baseline Values

To quantify the uncertainty in this experiment, five repeated measurements ($n = 5$) were taken for each test sample, ensuring to reduce and then reestablish the required Reynolds number between measurements. The mean values of C_d and $C_{l(rms)}$ in each measurement are averaged to calculate $\bar{C}_d$ and $\bar{C}_{l(rms)}$, and standard deviations, σ_d and σ_l. A 95% coverage interval is created around these mean values based on their expanded uncertainties, U, given by $U = k\sigma/\sqrt{n}$ [44]. These expanded uncertainties are calculated using $n-1 = 4$ degrees of freedom (ν), and a corresponding coverage factor of $k = 2.78$ for the 95% coverage interval [44]. A summary of these values are given in Table 4, and can be used to quantify uncertainty in further tests of each sample.

Table 4. Summary of values calculated in the experimental uncertainty analysis.

Case	$\bar{C}_d$	$\bar{C}_{l(rms)}$	$U_{\bar{C}_d}$	$U_{\bar{C}_{l(rms)}}$
Smooth	1.17	0.117	0.03	0.01
SJO	1.22	0.182	0.06	0.01
PCO	0.99	0.029	0.03	0.003
SJPC	1.02	0.158	0.03	0.01

The baseline smooth case was tested at $Re = 2.0 \times 10^4$, 3.0×10^4, and 3.5×10^4. As expected in this flow regime, as Re increases, so too does $\bar{C}_d$ [1] (1.075–1.25). However, there is no discernible trend in values of $C_{l(rms)}$. The baseline values of $\bar{C}_d$ and $\bar{C}_{l(rms)}$ at $Re = 3.0 \times 10^4$ are $1.17 \pm 2.6\%$ and $0.117 \pm 8.5\%$, respectively, with a shedding frequency of approximately 15.75 Hz based on $U_\infty = 1.5$ m/s and a nominal $Sr = 0.21$. The PCO case was also tested at $Re = 3.0 \times 10^4$ as a second baseline case. Values of $\bar{C}_d$ and $\bar{C}_{l(rms)}$ for the PCO case were found to be $0.99 \pm 3\%$ and $0.029 \pm 10\%$, respectively. The PCO sample sees a 15.4% reduction in $\bar{C}_d$ and 75% reduction in $\bar{C}_{l(rms)}$ relative to the baseline case.

3.1.2. Combined Cases

One eccentric crank corresponding to $\bar{L}_o = 114$ was tested. The SJO and SJAP test samples were tested in a range of C_μ (9.2×10^{-3}–8.32×10^{-2}) values at $f^+ = 0.25$, 0.5 and 0.76. Due to limitations in the DC motor, only f^+ values below unity could be studied. The results of these tests can be seen in Figure 5. In all SJO cases, $\bar{C}_d$ increases relative to the smooth baseline, indicating that, for $f^+ < 1$, the SJ does not have a drag reducing effect. Addition of the porous coating in the SJPC case significantly reduces C_d compared to the SJO case, and all but one smooth baseline case (f^+ = 0.76). For both the SJO and SJPC, C_d increases with f^+ or C_μ. Crucially, however, $\bar{C}_d$ for the SJPC cases is not lower than $\bar{C}_d$ for the PCO baseline. While the overall drag reduction is hindered by the SJA, it is interesting to note that the addition of the porous coating still has a beneficial effect of around 19–20% drag reduction relative to only using a SJA. The mechanism of drag reduction offered by the SJA seems to work against that of the porous coating. Similar trends are seen for $\bar{C}_{l(rms)}$, where SJPC case values of $\bar{C}_{l(rms)}$ lie between the higher SJO values, and the lower PCO baseline value. Neither the SJO nor the SJPC results outperform the baseline smooth cylinder case.

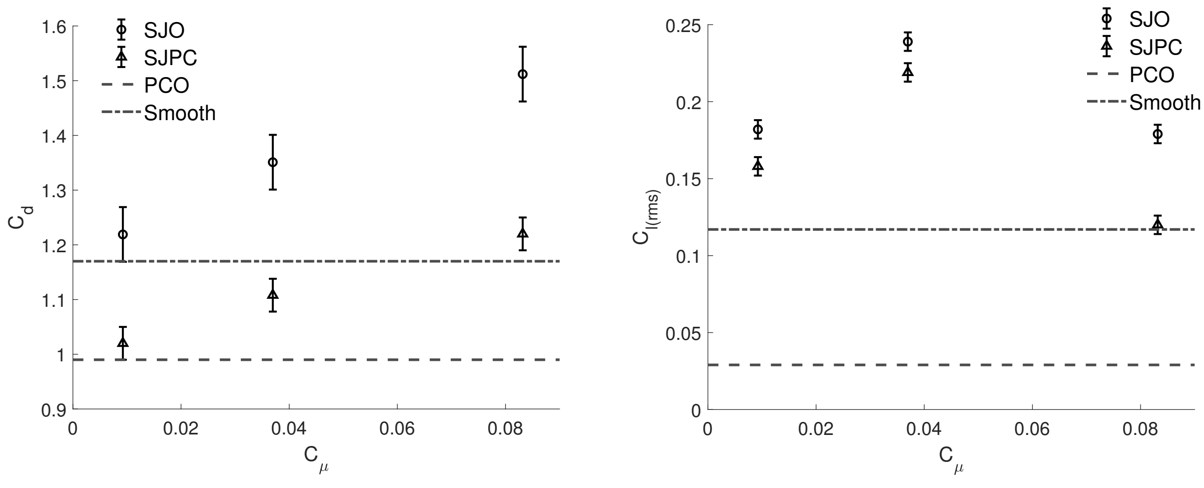

Figure 5. Averaged experimental results of drag and RMS lift coefficient as a function of momentum coefficient C_μ for each configuration, with error bars indicating experimental uncertainty. (**a**) C_d vs. C_μ and (**b**) $C_{l(rms)}$ vs. C_μ.

3.2. Numerical Results

The current SJPC numerical model was validated against the results of the experimental phase. Simulations of a SJPC with $\bar{L}_o$ = 144 and f = 4, 8, 12 and 16 Hz were carried out to mirror the experimental $\bar{L}_o$ and actuation frequencies. Figure 6 shows a good agreement between numerical and experimental C_d values when plotted against their respective C_μ values. This shows that the current SJPC model is capable of simulating the combined effect of the SJA and porous coating, and in fact appears to overpredict C_d.

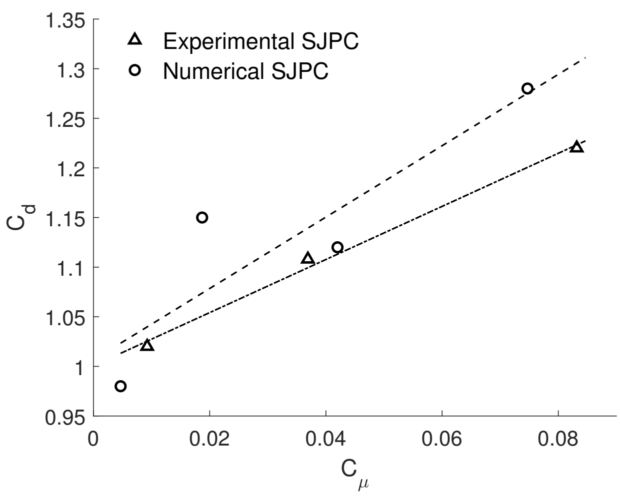

Figure 6. Comparison of experimental and numerical C_d values used for model validation.

3.2.1. Effect of f^+

The smooth and PCO cases at Re = 4.2 × 10^4 are used as baseline cases to compare to the SJPC model. Values of 0.15 < f^+ < 4 for C_μ = 3.6 × 10^{-3} were tested in the SJO and SJPC cases. The PCO has C_d = 0.763 which is a reduction of 35% compared to the smooth cylinder case and $C_{l(rms)}$ = 0.17 which is a 82% reduction. The surface distribution of C_p around SJPC models with f^+ = 0.15, 1, and 4 are compared to the smooth case and PCO case in Figure 7. It can be seen that the PCO causes a higher pressure on the lee of the cylinder compared to the smooth case, in line with the work of Klausmann and Ruck [10] and Guinness and Persoons [9].

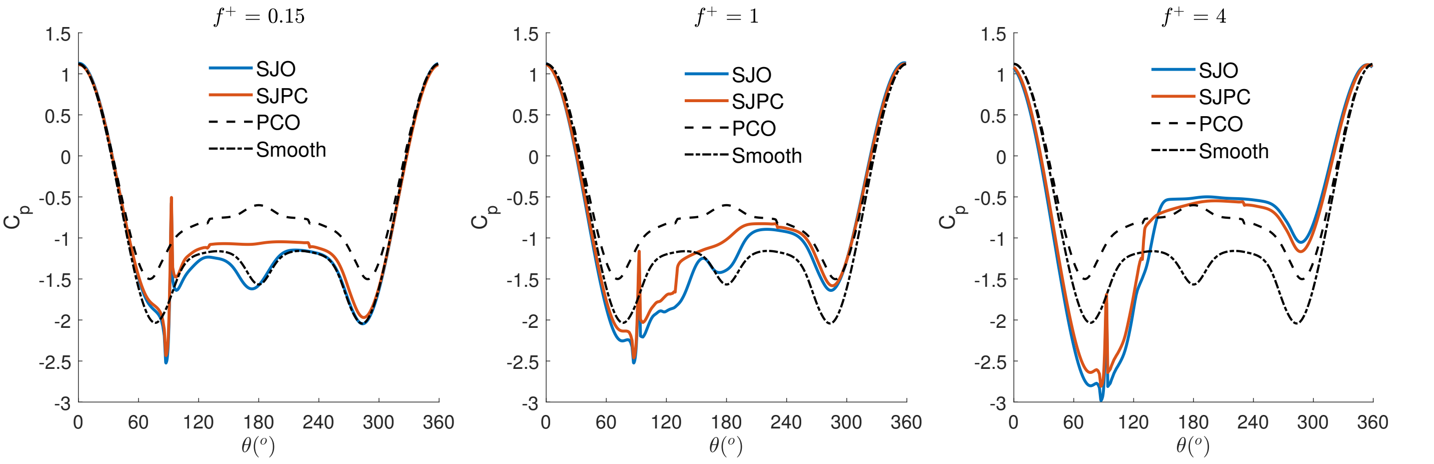

(**a**) (**b**) (**c**)

Figure 7. Distribution of pressure coefficient C_p around the cylinder for different SJA actuation frequencies (**a**) $f^+ = 0.15$, (**b**) $f^+ = 1$, and (**c**) $f^+ = 4$.

In the f^+ = 0.15 case (Figure 7a), the SJO causes no drag reduction and instead decreases leeward pressure on the side containing the SJA. The SJPC pressure distribution lies between the PCO and smooth cases, producing a drag reduction of 15%. This is significantly smaller than the reduction of the PCO case, indicating that the operation of the SJA in this condition hinders the effect of the porous coating. The f^+ = 1 case (Figure 7b) shows the behaviour of the models when the actuation frequency is equal to the natural shedding frequency. In both the SJO and SJPC, there is a large decrease in pressure just upstream and downstream of the SJA orifice. The pressure on the lower portion of the lee (180°–270°) is generally higher than the f^+ = 0.15 case. However, this increase does not counteract the decrease near the SJA, culminating in a higher C_d value of 1.24 for the SJO case. The f^+ = 4 case (Figure 7c) shows that at this operating condition, both the SJO and SJPC outperform the PCO case, with respective drag reductions of 46% and 45%. Despite the large pressure decrease either side of the SJA orifice, both cases increase the leeward pressure (130°–180°) more than in the PCO case. Both the SJO and SJPC cases have similar pressure distributions, indicating that the porous coating has less of an effect at this operating condition. For the f^+ = 4 cases, the value of C_μ was decreased to 1.8 × 10^{-3} to increase the influence of the porous coating in the SJPC case. This alteration had little effect on the values of C_d obtained (<1%) indicating that f^+ is the dominant parameter in the current setup. It was decided that future work could use alternate setups to better investigate the influence of C_μ.

Figure 8 compares the variation in C_d and $C_{l(rms)}$ with f^+ for each case tested. It is clear that below f^+ = 1, the SJO does not provide any drag reduction, with a maximum drag increase of 11%. The SJPC, however, provides a drag reduction in every case below f^+ = 1, albeit a smaller drag reduction than the PCO case. Above f^+ = 1, there is drag reduction in each SJO and SJPC case tested referenced to the smooth case, with an optimum reduction at f^+ = 4. Drag decreases with actuation frequency above f^+ = 1. However, a wider range of f^+ values needs to be studied to determine whether drag reduction is saturated beyond this point. In terms of altering lift forces, there is no discernible trend in $C_{l(rms)}$ below f^+ = 1, with the SJPC providing $C_{l(rms)}$ decreases for the lower actuation frequencies and increases for higher frequencies. The SJO shows the exact opposite trend. Above f^+ = 1, there is a minimum value in $C_{l(rms)}$, offering a 22% reduction for both the SJO and SJPC cases, before a gradual increase $C_{l(rms)}$ with f^+. While both the SJO and SJPC cases at f^+ = 2, 3 give very similar $C_{l(rms)}$ values, there is a significant difference at f^+ = 4, with the SJPC offering a much lower $C_{l(rms)}$ value (1.1) than the SJO case (1.33).

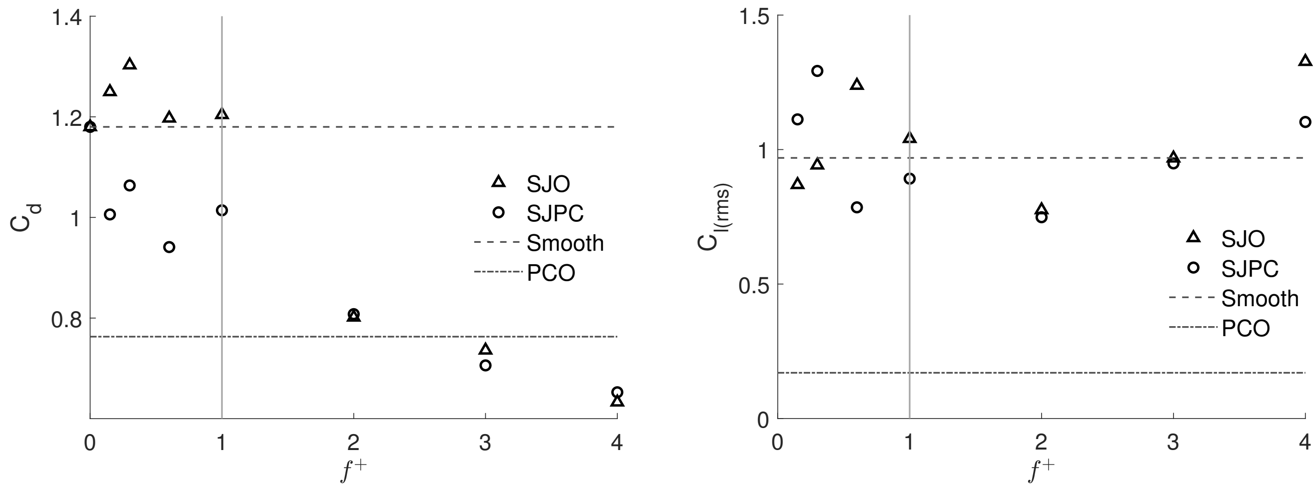

(**a**) (**b**)

Figure 8. Numerical results for the dependence of drag and lift coefficient as a function of SJA frequency for each configuration: (**a**) C_d vs. f^+ and (**b**) $C_{l(rms)}$ vs. f^+.

3.2.2. Flow Field and Wake Behaviour

This section discusses the flow field of the SJPC model compared to the PCO and SJO cases. Figure 9 compares the velocity flow fields of three cases at maximum ejection and ingestion. These three cases are SJPC for $f^+ = 4$, $f^+ = 1$ and the SJO case for $f^+ = 1$. The different behaviour of the SJ across the cases studied can be clearly seen. It is interesting to note that there is less of an interaction between the SJ and the porous layer in the $f^+ = 4$ case compared to the $f^+ = 1$ case. Figure 10a compares the flow field of the SJPC at f^+ = 4 (top) and the PCO (bottom) at the moment a vortex is being shed. The porous coating in the PCO case clearly works to significantly delay vortex shedding, which increases the leeward pressure [10,32]. This increase in leeward pressure is clear in Figure 7c. Neither the flowfield nor the C_p distribution of the SJPC and SJO at f^+ = 4 differed significantly, meaning that the flowfield of the SJPC in Figure 10a is controlled primarily by the SJA. The SJPC in this setup has a separation angle of 104° case. This delay in boundary layer separation narrows the wake compared to the PCO case. Similar to the PCO case, the SJA appears to delay vortex shedding. This effect was also seen in the SJO flowfield for f^+ = 4.

An interesting case is the difference in C_d between the SJO and SJPC cases at f^+ = 1, where the SJO caused drag increase and the SJPC caused drag reduction. This can be explained by viewing Figure 10b, which compares the time-averaged flow-field of velocity magnitude for the SJO and SJPC at f^+ = 1. The porous coating in the SJPC case increases the extent of the re-circulation zone in the wake by about 0.5D compared to the SJO case. This increased re-circulation zone corresponds to a delaying of vortex shedding and increase in leeward pressure, explaining the lower C_d in the SJPC case. A comparison between the SJO and SJPC models at f^+ = 1 and f^+ = 4 was made to explain the superior drag reduction effects at f^+ = 4. The time-averaged turbulence intensity, I, was monitored at downstream locations of x/D = 1.5, 2.5 and 3.5. The results of this analysis are shown in Figure 11a. In each case, it appears that the SJO causes slightly larger levels of turbulence intensity than the SJPC. For $f^+ = 4$, there is significantly larger turbulence intensity, with a maximum value of 0.34 in the SJO at $x/D = 1.5$, compared to a maximum of 0.134 in the corresponding $f^+ = 1$ case. The wake widths of the $f^+ = 4$ cases are qualitatively narrower at each x/D location than the $f^+ = 1$ cases. This narrower wake corresponds to a higher leeward pressure and lower C_d value, explaining the superior drag reduction at $f^+ = 4$. To confirm this, the relationship between wake width, w, and C_d is investigated by comparing all SJO and SJPC cases of $f^+ \geq 1$. Wake width is measured at $x/D = 1.5$ between points of half the maximum turbulence intensity. The wake width in the smooth and PCO baseline cases is $1.52D$ and $1.23D$ respectively. Figure 11b shows the results of this analysis. There is a clear proportional relationship between C_d and wake width. Since C_d decreases with f^+ in the region $1 < f^+ < 4$, it is clear that the wake width also decreases with f^+ in this region.

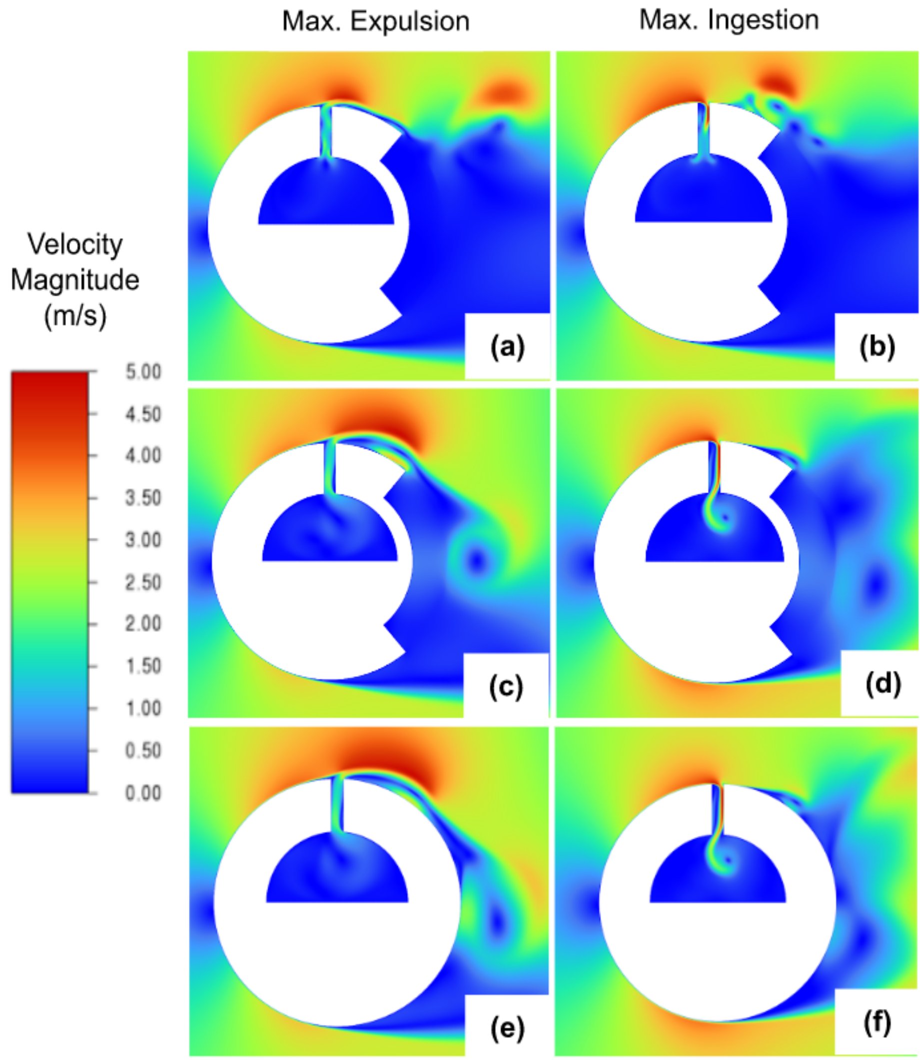

Figure 9. Comparison of instantaneous flow velocity fields at a phase angle corresponding to (**a**,**c**,**e**) maximum expulsion and (**b**,**d**,**f**) maximum ingestion of the synthetic jet: (**a**,**b**) SJPC at $f^+ = 4$, (**c**,**d**) SJPC at $f^+ = 1$, (**e**,**f**) SJO at $f^+ = 1$.

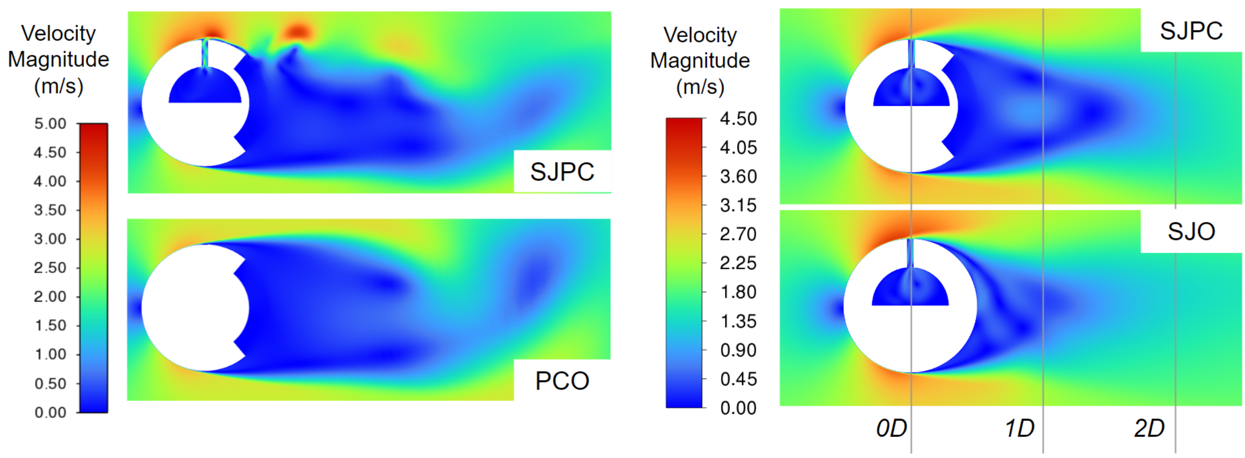

(**a**) (**b**)

Figure 10. Comparison of flow-fields of velocity magnitude: (**a**) Instantaneous flow-field for SJPC at f^+ = 4 and PCO at comparable instants in the wake vortex roll-up period. (**b**) Time-averaged flow-field for SJPC and SJO at f^+ = 1.

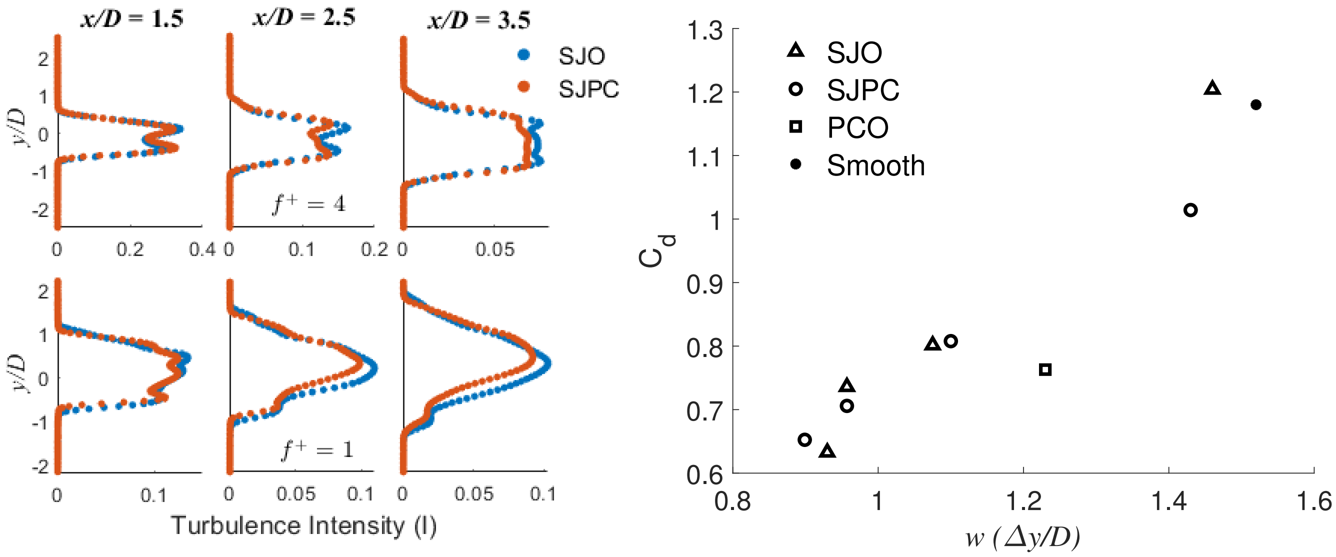

(**a**) (**b**)

Figure 11. Summary of wake analysis: (**a**) Turbulence intensity comparison in wake of SJPC at $f^+ = 4$ (top) and $f^+ = 1$ (bottom) at downstream locations $x/D = 1.5, 2.5, 3.5$. (**b**) Relationship between C_d and wake width w for $f^+ > 1$.

4. Discussion

The experimental phase of this current study showed that a 100° porous coating on the lee of a cylinder in crossflow (Re = 4.2 × 10^4) causes a nominal reduction in C_d of 15% compared to a reference cylinder. This agrees well with the experimental findings of Klausmann and Ruck [10], who obtained a 13% reduction in drag for the same coating angle. The experimental results showed that, for $f^+ \leq 1$, the SJO produces an increase in drag relative to a reference cylinder. This agrees with Tensi et al. [23], who showed experimentally that increasing C_μ and f^+ increases C_d for $f^+ \leq 1$. As for the current experimental study, Tensi et al. [23] did not decouple C_μ and f^+. The current experimental results show that the SJPC can achieve a drag reduction of 12.8% relative to a reference cylinder with no SJPC test achieving a larger drag reduction than the PCO sample within the parameters tested. This is an indication that the porous coating is useful for reducing the negative drag increase effect of the SJA in this range ($f^+ < 1$). A similar trend is seen for $C_{l(rms)}$, in which the SJPC produces lower $C_{l(rms)}$ values than the SJO sample, demonstrating the ability of the porous coating to reduce aerodynamic lift oscillations. Further experiments should investigate the effect of SJPC samples at $f^+ > 1$ to improve the validation of the numerical model. It should be ensured in future work that the effect of C_μ and f^+ are decoupled.

The current numerical results show that combining a porous coating with a SJA reduces the increase in C_d associated with the SJA for $f^+ \leq 1$. As shown in Figure 8a, the SJO increases C_d for all $f^+ < 1$. However, the added porous coating in the SJPC cases shows a consistent 15–21% reduction in C_d relative to corresponding SJO cases in this f^+ region. This can be attributed to the porous coating delaying vortex shedding and causing an increase in leeward pressure on the cylinder. The effect of combining the porous coating and SJA on $C_{l(rms)}$ in this region is less clear, however. For $f^+ = 0.15$ and 0.3, the SJO produces lower $C_{l(rms)}$ values, whereas for $f^+ = 0.6$ and 1, the SJPC produces lower $C_{l(rms)}$ values. The unexpected results for $f^+ = 0.15$ and 0.3, in which the porous coating acts to increase $C_{l(rms)}$, may be due to complex interactions between the SJA and cylinder vortex shedding, with the former having a much larger timescale than the latter. For $f^+ > 1$, there appears to be no benefit in combining the porous coating and SJA in terms of drag reduction. While in the $f^+ \leq 1$ region, the addition of a porous coating provided a reduction in drag across all cases relative to the SJO cases, this trend is broken at higher f^+ values. While the SJO model offers drag reduction at $f^+ = 2$, it is still inferior to the PCO model. The SJPC produces an almost identical C_d value to the SJO at this f^+ value, demonstrating two things: (i) even when the SJA on its own is capable of significant drag reduction, it still does not combine constructively with the porous coating to obtain superior drag reduction and (ii) at f^+ values above 1, the flow control effect of the SJA dominates and the addition of the porous coating has little to no effect. It should be noted that there seems to be a suggestion that the addition of the porous coating at $f^+ = 4$ causes a reduction in $C_{l(rms)}$. While the range of f^+ studied was limited, the optimum drag reduction of 46% using the SJO occured at $f^+ = 4$, in agreement with low f^+ ranges studied by Fujisawa and Takeda [5] and Glezer et al. [25].

As stated in the literature on porous coatings [9,10,29–32], the delaying in vortex shedding which increases leeward pressure is caused by low-momentum fluid emerging from the porous coating into the wake, which acts to stabilise the shear layers. Based on this explanation of the porous coating drag reduction mechanism, it is perhaps not surprising that, in the SJPC cases for $f^+ \leq 1$, while drag reduction is achieved, it is inferior to the drag reduction of the PCO model. As the porous coating acts to stabilise shear layers, the SJA acts to disturb them by adding momentum in an attempt to delay boundary layer separation. This can explain the reduced effectiveness of the porous coating in the SJPC model compared to the PCO model. A similar effect is seen at $f^+ = 2$, in which the operation of the SJA acts to reduce the effectiveness of the porous coating in the SJPC case. For $f^+ > 1$, the dominant mechanism of flow control is that of the SJA, in which a delay in boundary layer separation causes an increase in leeward pressure, decreasing pressure drag. This is confirmed by the analysis of wake widths, w, for the $f^+ \geq 1$ region, which showed that the reduction in drag correlated to a decrease in wake width. Analysis of the flow fields and turbulence intensity in the wake showed that there was little difference between the SJO and SJPC models for $f^+ > 1$, indicating that once the SJA becomes capable of reducing drag, the presence of the porous coating has little to no effect. It appears that for this SJA angle of $\theta = 90°$, the mechanisms by which the SJA and porous coating reduce drag seem to be incapable of combining constructively for enhanced drag reduction. However, as discussed, there are benefits to the addition of the porous coating for $f^+ \leq 1$, and a possible benefit in terms of $C_{l(rms)}$ reduction at $f^+ \leq 4$. Further research should be conducted at larger f^+ values to investigate this benefit. There is also good reason to investigate a combined SJA and porous coating with the SJA at different angles. For example, the base bleed effect of the porous coating may be enhanced by placing the SJA at $\theta = 180°$.

5. Conclusions

The current study has created a numerical model which simulates the combined effect on drag and lift forces of a synthetic jet actuator (SJA) at θ = 90° and a 100° wide leeward porous coating embedded in a cylinder in crossflow of $Re = 4.2 \times 10^4$. This model has been validated experimentally by means of water tunnel testing. Numerical findings show that for $f^+ < 1$, the combined synthetic jet/porous coating (SJPC) configuration has a consistent 15–21% reduction in C_d compared to the synthetic jet only (SJO) configuration at the same f^+ values. This demonstrates the benefit of adding a leeward porous coating to a cylinder containing a SJA for $f^+ < 1$, as it can offer a drag reduction relative to a reference cylinder, which was not possible with only a SJA at θ = 90° in this f^+ region. Instead, the SJA was shown to increase C_d for $f^+ < 1$, suggesting its flow control mechanism does not seem to be active at these settings. The porous coating, however, provides passive flow control by stabilising the shear layers and delaying vortex shedding, reducing the unwanted drag increase of the SJA. Experimental results confirm the beneficial effect of the porous coating on the SJA for $f^+ < 1$.

By contrast, at higher frequencies ($f^+ > 1$), the SJPC and SJO models behave almost identically in terms of their effect on C_d and $C_{l(rms)}$, aside from a small reduction in $C_{l(rms)}$ offered by the SJPC model at $f^+ = 4$. By analysing the flow fields and wakes of both models, it was found that the drag reduction comes from a narrowing of the wake, increasing the leeward pressure. This behaviour suggests that the primary reason for drag reduction is the SJA at $f^+ > 1$, and that the porous coating has almost no role in drag reduction in the combined models in this f^+ region.

Both the experimental and numerical results showed that, across the parameters tested in this study, there was no constructive combined effect of the SJA and porous coating, in that no SJPC case provided a lower C_d value than those of the SJA and porous coating implemented on their own. While the porous coating offers benefits in the SJPC model for $f^+ < 1$, the maximum drag reduction of this model is only 20% compared to the 35% reduction offered by using only the porous coating. A maximum drag reduction of 46% was found using the SJO model at $f^+ = 4$.

In summary, the porous coating reduces the negative flow control aspects of using only a SJA at $f^+ < 1$. However, the drag and lift reduction mechanisms seem to act destructively at $f^+ < 1$, with the SJA weakening the potential drag reduction of the porous coating. The SJA seems to dominate the control of the flow field for $f^+ > 1$. It should be noted that this study has only investigated an SJA at θ = 90°. As such, there is potential for some beneficial combined base bleed effect at other SJA angles, e.g., θ = 180°.

Author Contributions: Conceptualization, T.P., M.G. and G.F.; methodology, G.F.; software, G.F.; validation, G.F.; formal analysis, G.F.; investigation, G.F.; data curation, G.F.; writing—original draft preparation, G.F.; writing—review and editing, G.F., T.P. and M.G.; visualization, G.F.; supervision, T.P. and M.G. All authors have read and agreed to the published version of the manuscript.

Funding: This research received no external funding.

Institutional Review Board Statement: Not applicable.

Informed Consent Statement: Not applicable.

Data Availability Statement: Not applicable.

Acknowledgments: The authors gratefully acknowledge Gerry Byrne for his help in setting up and maintaining the experimental rig used in this study, and John Kennedy for his help developing the porous coatings and providing SLA printers.

Conflicts of Interest: The authors declare no conflict of interest.

Abbreviations

The following abbreviations are used in this manuscript:

SJA	Synthetic jet actuator
SJ	Synthetic jet
RMS	Root-mean-square
VR	Velocity ratio
PPI	Pores per inch
FDM	Fused deposition modelling
SLA	Stereolithography
URANS	Unsteady Reynolds-averaged Navier-Stokes
SST	Shear stress transport
UDF	User-defined function
SJPC	Combined SJA and porous coating configuration
PCO	Porous coating only configuration
SJO	SJA only configuration

Appendix A. Actuator Surface UDF

```
#include "udf.h"
DEFINE_PROFILE(unsteady_velocity, thread, position)
{
face_t f;
real t = CURRENT_TIME;
real V_max, L, freq, pi, time, h, d;

d = 0.08695;
pi = 3.14159;
freq = 4;
L = 0.0571*2;
V_max = L*freq*pi*d;

begin_f_loop(f, thread)
{
F_PROFILE(f, thread, position) = V_max*sin(2*pi*freq*t);
}
end_f_loop(f, thread)
}
```

References

1. Munson, B.; Rothmayer, A.; Okiishi, T.; Huebsch, W. *Fundamentals of Fluid Mechanics*, 7th ed.; Wiley: Hoboken, NJ, USA, 2013.
2. Gad-el Hak, M.; Gad-El-Hak, C. *Flow Control: Passive, Active, and Reactive Flow Management*; Cambridge University Press: Cambridge, UK, 2000.
3. Shehata, A.; Xiao, Q.; Saqr, K.; Naguib, A.; Alexander, D. Passive flow control for aerodynamic performance enhancement of airfoil with its application in Wells turbine—Under oscillating flow condition. *Ocean. Eng.* **2017**, *136*, 31–53. [CrossRef]
4. Amitay, M.; Honohan, A.; Trautman, M.; Glezer, A. Modification of the aerodynamic characteristics of bluff bodies using fluidic actuators. In Proceedings of the 28th Fluid Dynamics Conference 28th Fluid Dynamics Conference, Snowmass Village, CO, USA, 29 June–2 July 1997. [CrossRef]
5. Fujisawa, N.; Takeda, G. Flow control around a circular cylinder by internal acoustic excitation. *J. Fluids Struct.* **2003**, *17*, 903–913. [CrossRef]
6. Catalano, P.; Wang, M.; Iaccarino, G.; Sbalzarini, I. Optimization of cylinder flow control via zero net mass flux actuators. In *Center for Turbulence Research Summer Program*; Wiley: Stanford, CA, USA, 2002; Available online: https://onlinelibrary.wiley.com/doi/epdf/10.1002/fld.4755 (accessed on 10 June 2022).
7. Greco, C.S.; Paolillo, G.; Astarita, T.; Cardone, G. The von Kármán street behind a circular cylinder: Flow control through synthetic jet placed at the rear stagnation point. *J. Fluid Mech.* **2020**, *901*, A39. [CrossRef]
8. Zhang, P.; Liu, Y.; Li, Z.; Liu, H.; Yang, Y. Numerical study on reducing aerodynamic drag and noise of circular cylinders with non-uniform porous coatings. *Aerosp. Sci. Technol.* **2020**, *107*, 106308. [CrossRef]

9. Guinness, I.; Persoons, T. Passive flow control for drag reduction on a cylinder in cross-flow using leeward partial porous coatings. *Fluids* **2021**, *6*, 289. [CrossRef]
10. Klausmann, K.; Ruck, B. Drag reduction of circular cylinders by porous coating on the leeward side. *J. Fluid Mech.* **2017**, *813*, 382–411. [CrossRef]
11. Bruneau, C.; Mortazavi, I. Control of vortex shedding around a pipe section using a porous sheath. *Int. J. Offshore Polar Eng.* **2006**, *16*, 90–96.
12. Bathla, P.; Kennedy, J. 3D printed structured porous treatments for flow control around a circular cylinder. *Fluids* **2020**, *5*, 136. [CrossRef]
13. Smith, B.; Glezer, A. The formation and evolution of synthetic jets. *Phys. Fluids* **1998**, *10*, 2281–2297. [CrossRef]
14. Hong, M.; Cheng, S.; Zhong, S. Effect of geometric parameters on synthetic jet: A review. *Phys. Fluids* **2020**, *32*, 031301. [CrossRef]
15. Auerbach, D. Experiments on the trajectory and circulation of the starting vortex. *J. Fluid Mech.* **1987**, *183*, 185–198. [CrossRef]
16. Feng, L.; Wang, J. Synthetic jet control of separation in the flow over a circular cylinder. *Exp. Fluids* **2012**, *53*, 467–480. [CrossRef]
17. Holman, R.; Utturkar, Y.; Mittal, R.; Smith, B.; Cattafesta, L. Formation criterion for synthetic jets. *AIAA J.* **2005**, *43*, 2110–2116. [CrossRef]
18. Jabbal, M.; Zhong, S. The near wall effect of synthetic jets in a laminar boundary layer. In Proceedings of the 3rd AIAA Flow Control Conference, San Francisco, CA, USA, 5–8 June 2006. [CrossRef]
19. Sahni, O.; Wood, J.; Jansen, K.E.; Amitay, M. Three-dimensional interactions between a finite-span synthetic jet and a crossflow. *J. Fluid Mech.* **2011**, *671*, 254–287. [CrossRef]
20. Rathay, N.; Amitay, M. Interaction of synthetic jets with a massively separated three-dimensional flow field. *Phys. Rev. Fluids* **2022**, *7*, 034702. [CrossRef]
21. Chiatto, M.; Marchitto, L.; Valentino, G.; de Luca, L. Influence of piezo-driven synthetic jet on water spray behavior. *At. Sprays* **2017**, *27*, 691–706. [CrossRef]
22. Feng, L.; Wang, J. Modification of a circular cylinder wake with synthetic jet: Vortex shedding modes and mechanism. *Eur. J. Mech.—B/Fluids* **2014**, *43*, 14–32. [CrossRef]
23. Tensi, J.; Boué, I.; Paillé, F.; Dury, G. Modification of the wake behind a circular cylinder by using synthetic jets. *J. Vis.* **2002**, *5*, 37–44. [CrossRef]
24. Hsiao, F.; Shyu, J. Influence of internal acoustic excitation upon flow passing a circular cylinder. *J. Fluids Struct.* **1991**, *5*, 427–442. [CrossRef]
25. Glezer, A.; Amitay, M.; Honohan, A. Aspects of low- and high-frequency actuation for aerodynamic flow control. *AIAA J.* **2005**, *43*, 1501–1511. [CrossRef]
26. Bruneau, C.; Mortazavi, I.; Gilliéron, P. Flow regularisation and drag reduction around blunt bodies using porous devices. In Proceedings of the IUTAM Symposium on Flow Control and MEMS, London, UK, 19–22 September 2006; Springer: Dordrecht, The Netherlands, 2006; Volume 7.
27. Teruna, C.; Avallone, F.; Ragni, D.; Casalino, D. On the noise reduction of a porous trailing edge applied to an airfoil at lifting condition. *Phys. Fluids* **2021**, *33*, 055132. [CrossRef]
28. Bhattacharyya, S.; Singh, A. Reduction in drag and vortex shedding frequency through porous sheath around a circular cylinder. *Int. J. Numer. Methods Fluids* **2011**, *65*, 683–698. [CrossRef]
29. Sueki, T.; Takaishi, T.; Ikeda, M.; Arai, N. Application of porous material to reduce aerodynamic sound from bluff bodies. *Fluid Dyn. Res.* **2010**, *42*, 015004. [CrossRef]
30. Hu, Z.; Liu, H.; Chen, N.; Hu, J.; Tong, F. Vortex shedding noise and flow mode analysis of cylinder with full/partial porous coating. *Aerosp. Sci. Technol.* **2020**, *106*, 106154. [CrossRef]
31. Naito, H.; Fukagata, K. Numerical simulation of flow around a circular cylinder having porous surface. *Phys. Fluids* **2012**, *24*, 117102. [CrossRef]
32. Galbraith, R. Flow pattern around a shrouded cylinder at Re = 5000. *J. Wind. Eng. Ind. Aerodyn.* **1980**, *6*, 227–242. [CrossRef]
33. Igarashi, T. Flow characteristics around a circular cylinder with a slit: 1st report, flow control and flow patterns. *Bull. JSME* **1978**, *21*, 656–664. [CrossRef]
34. Steiros, K.; Bempedelis, N.; Ding, L. Recirculation regions in wakes with base bleed. *Phys. Rev. Fluids* **2021**, *6*, 034608. [CrossRef]
35. Jackson, D. Active Flow Control of a Cylinder in Crossflow using Synthetic Jet Actuators. Ph.D. Thesis, Trinity College Dublin, Dublin, Ireland, 2016. Available online: http://www.tara.tcd.ie/handle/2262/82914 (accessed on 15 July 2022).
36. Argyropoulos, C.; Markatos, N. Recent advances on the numerical modelling of turbulent flows. *Appl. Math. Model.* **2015**, *39*, 693–732. [CrossRef]
37. Rosetti, G.; Vaz, G.; Fujarra, A. URANS calculations for smooth circular cylinder flow in a wide range of Reynolds numbers: Solution verification and validation. *J. Fluids Eng.* **2012**, *134*, 121103. [CrossRef]
38. ANSYS. *ANSYS Fluent User's Guide*; ANSYS: Canonsburg, PA, USA, 2021.
39. Alimohammadi, S.; Fanning, E.; Persoons, T.; Murray, D. Characterization of flow vectoring phenomenon in adjacent synthetic jets using CFD and PIV. *Comput. Fluids* **2016**, *140*, 232–246. [CrossRef]
40. Jain, M.; Puranik, B.; Agrawal, A. A numerical investigation of effects of cavity and orifice parameters on the characteristics of a synthetic jet flow. *Sens. Actuators A Phys.* **2011**, *165*, 351–366. [CrossRef]

41. Freitas, C. Verification and validation in computational fluid dynamics and heat transfer: PTC 61. In Proceedings of the ASME 2006 Power Conference, Atlanta, GA, USA, 2–4 May 2006; pp. 793–800. [CrossRef]
42. Liu, H.; Wei, J.; Qu, Z. The interaction of porous material coating with the near wake of bluff body. *J. Fluids Eng.* **2013**, *136*, 021302. [CrossRef]
43. Roshko, A. Experiments on the flow past a circular cylinder at very high Reynolds number. *J. Fluid Mech.* **1961**, *10*, 345–356. [CrossRef]
44. Kirkup, L.; Frenkel, R.B. The t-distribution and Welch-Satterthwaite formula. In *An Introduction to Uncertainty in Measurement: Using the GUM (Guide to the Expression of Uncertainty in Measurement)*; Cambridge University Press: Cambridge, UK, 2006; pp. 162–190. [CrossRef]